

Article

Analysis of Damage to Reinforced Concrete Beams Under Explosive Effects of Different Shapes, Equivalents, and Distances

Yu Ma ¹, Rongyue Zheng ^{1,2,*}, Wei Wang ² , Chenzhen Ye ^{1,*}, Wenzhe Luo ¹ and Sihao Shen ²

¹ School of Civil & Environmental Engineering and Geography Science, Ningbo University, Ningbo 315211, China; 2211110077@nbu.edu.cn (Y.M.); 2211110076@nbu.edu.cn (W.L.)

² Key Laboratory of Impact and Safety Engineering, Ningbo University, Ningbo 315211, China; wangwei7@nbu.edu.cn (W.W.); 2211090026@nbu.edu.cn (S.S.)

* Correspondence: zhengrongyue@nbu.edu.cn (R.Z.); yechenzhen@nbu.edu.cn (C.Y.)

Abstract: Optimizing structural resistance against blast loads critically depends on the effects of different explosive shapes, equivalents, and distances on the damage characteristics of reinforced concrete beams. This study bridges the knowledge gap in understanding how these factors influence damage mechanisms through close-range air blast experiments and LS-DYNA numerical simulations. Key damage characteristics, such as craters, overpressure, impulse, time-history displacement, and residual mid-span displacement of reinforced concrete beams, were thoroughly analyzed. Results show that cuboid-shaped explosives cause the greatest damage, with the most severe effects observed at shorter distances and higher charge weights, including an increase in mid-span displacement of up to 16.3 cm. The study highlights the pivotal role of explosive geometry, charge weight, and standoff distance in shock wave propagation and structural failure and proposes an optimized damage criterion to enhance predictive capabilities for reinforced concrete beams under blast loads.

Keywords: reinforced concrete beam; explosive shape; near-field explosion; damage criteria



Academic Editor: Grzegorz Ludwik Golewski

Received: 30 December 2024

Revised: 16 January 2025

Accepted: 20 January 2025

Published: 31 January 2025

Citation: Ma, Y.; Zheng, R.; Wang, W.; Ye, C.; Luo, W.; Shen, S. Analysis of Damage to Reinforced Concrete Beams Under Explosive Effects of Different Shapes, Equivalents, and Distances. *Buildings* **2025**, *15*, 452. <https://doi.org/10.3390/buildings15030452>

Copyright: © 2025 by the authors. Licensee MDPI, Basel, Switzerland. This article is an open access article distributed under the terms and conditions of the Creative Commons Attribution (CC BY) license (<https://creativecommons.org/licenses/by/4.0/>).

1. Introduction

In contemporary society, peace and development remain prevailing themes. However, the global rise of extremism and terrorism has led to frequent local conflicts and attacks on civilians. Explosive attacks, driven by the simplicity of manufacturing explosives and the widespread availability of weapons, have become a primary tactic of modern terrorism. Reinforced concrete beams are widely used due to their strong plasticity, good integrity, and fire resistance. As key structural components of buildings, reinforced concrete beams are particularly vulnerable to the effects of near-field explosions. Unlike distant blasts, near-field explosions generate unevenly distributed loads, with high-intensity shock waves causing severe localized damage. Studying the damage characteristics of reinforced concrete beams under explosive conditions is essential for assessing structural vulnerability and improving safety designs [1–8].

In explosion tests on reinforced concrete beams, various parameters, including explosive equivalent, scaled distance, and the strength of reinforcement and concrete, influence their response and damage characteristics under explosive loads [9]. Scholars, both domestically and internationally, have studied how different factors affect the damage characteristics of beams. Chaozhi Yang [10] conducted explosion tests to analyze the effects of explosive weight, and developed a semi-empirical equation based on a dimensional analysis to calculate the span of the damage zone. His results showed a clear correlation

between the explosive weight and the extent of the damage, providing valuable insight into the dynamic fracture behavior of reinforced concrete structures. Yan Liu [11] conducted experimental and analytical research on the explosive performance of RC beams, introducing a coefficient that accounts for both explosion distance and scaled distance. This coefficient addresses the variation in beam damage due to changes in the explosion distance, emphasizing the significant impact of distance on the extent of damage. However, research on the effects of explosive shape on the damage characteristics of reinforced concrete beams remains relatively scarce. Most existing studies primarily focus on factors such as explosive equivalent and standoff distance, while the specific influence of explosive shape on blast wave propagation and destructive effects has not been thoroughly explored. Chu Gao [12] conducted explosion shock wave experiments in concrete using cylindrical charges. Numerical studies have analyzed how blast waves from spherical and cylindrical charges, with different length-to-diameter ratios, weaken in a concrete environment, focusing on the decrease in wave intensity over distance. His findings emphasized that the shape of the explosive charge plays a crucial role in determining the blast wave's intensity and its interaction with concrete structures. In damage assessment, Wei Wang [13] investigated the damage criteria of RC beams under blast wave effects by observing the failure modes and characteristics of beams subjected to varying charge amounts. He established and refined damage criteria, providing valuable references for engineering applications and damage assessment. Additionally, current damage criteria often fail to account for variations in explosive shape, a phenomenon which may lead to insufficient accuracy and comprehensiveness in damage assessments. Therefore, further investigation into the impact of explosive shape and its incorporation into damage criteria is crucial for enhancing and refining the existing explosion damage evaluation framework.

To address the gaps in the existing research, this study first conducted four sets of close-range airburst experiments involving different explosive shapes, equivalents, and standoff distances to investigate their effects on the damage of RC beams. Subsequently, 14 groups of numerical simulations were carried out using LS-DYNA to validate and analyze the damage characteristics of reinforced concrete beams under different explosives, including crater formation, overpressure, impulse, time-history displacement, and residual mid-span displacement. Based on the results of these experiments and simulations, this study proposes an optimized damage criterion that comprehensively accounts for the influence of explosive shape, equivalent, and standoff distance on structural damage. This criterion provides a more precise standard for assessing the damage of RC beams under various explosive conditions. Its introduction contributes to improving methods for predicting structural damage caused by blast waves and offers more targeted guidance for the design of blast-resistant concrete beams.

2. Explosion Tests

2.1. Overview of the Experiment

Three identical reinforced concrete beams were designed and fabricated as test specimens to simulate the mechanical response and failure traits of RC beams under practical application scenarios, in accordance with the GB50020-2010 Code for Construction of Concrete Structures. The beams had a cross-sectional dimension of 3000 mm × 125 mm × 250 mm, with a fixed span of 2500 mm.

The tension reinforcement consisted of four HRB400-grade steel bars with a diameter of 10 mm, while the compression reinforcement included two HRB400-grade steel bars of the same diameter. Additionally, the stirrups were made of HRB335-grade steel bars with a diameter of 6 mm, spaced at 100 mm intervals. HRB400 refers to hot-rolled ribbed steel reinforcement with a nominal yield strength of 400 MPa, while HRB335 represents

hot-rolled ribbed steel bars with a specified yield strength of 335 MPa. The concrete used was of strength grade C40, with a protective layer thickness of 20 mm. The reinforcement details and dimensions are shown in Figure 1, illustrating the specific arrangement of the steel bars. The explosive masses in Table 1 (2 kg, 6 kg, and 10 kg) were chosen to represent a range of typical explosion scenarios relevant to structural safety research. The distance also significantly influences the destructive power. Therefore, the selection of explosive equivalent and distance was based on Wei Wang's [13] damage criteria standards.

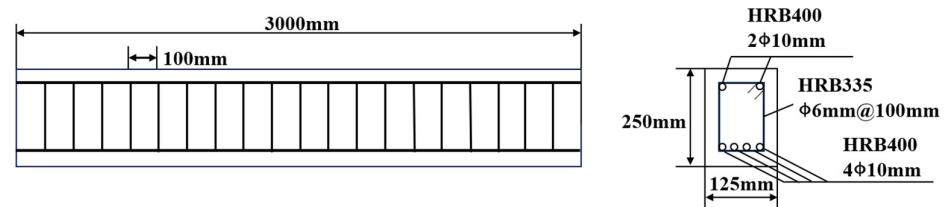


Figure 1. Reinforcement diagram of the reinforced concrete beam.

Figure 2 illustrates the schematic layout of the explosion test setup for the reinforced concrete beam. The setup primarily consisted of supports, steel plates, brackets, explosives, ropes, and the reinforced concrete beam. The height of the support was 1000 mm, elevating the beam above the ground to prevent the impact of ground reflection overpressure on the beam. To prevent the beam from being displaced due to the explosive's power, steel plates and bolts were used to clamp the beam at both ends, creating fixed boundary conditions. A bracket was erected behind the test site to suspend the explosives, ensuring they were positioned at the predetermined location and height before detonation. The on-site arrangement is shown in Figure 3.

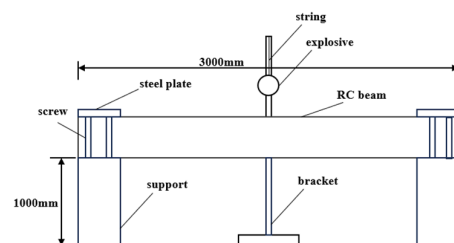


Figure 2. Schematic diagram of the experimental setup.



Figure 3. On-site layout diagram.

For the selection of the explosives, No. 2 rock emulsion explosives with a stable performance and moderate power were used. Considering the impact of explosive standoff distance, equivalent, and shape on the test results, four different test schemes were designed, as shown in Table 1. These schemes cover explosives of different weights, shapes, and sizes to comprehensively evaluate their effects on the damage to reinforced concrete beams. The shapes and dimensions of the explosives are shown in Figure 4.

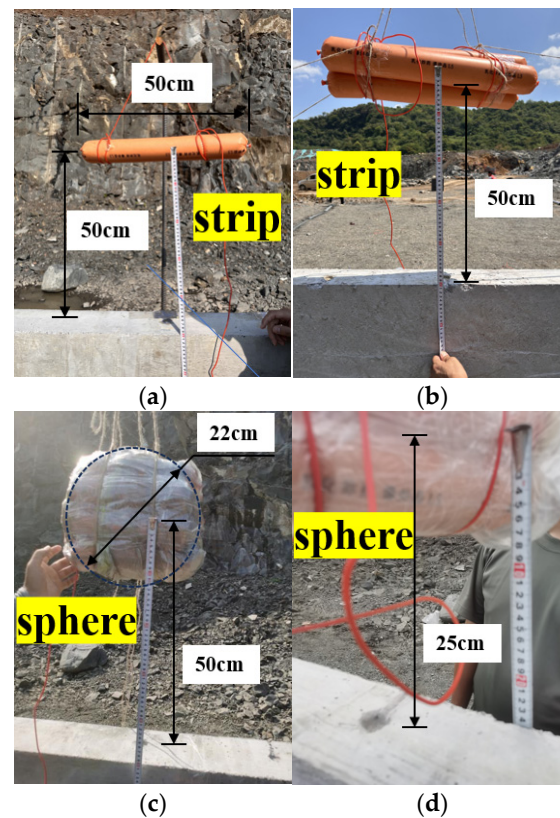


Figure 4. Explosive arrangement diagram for the experiment (a) S-1 test, 2 kg, 50 cm, (b) S-2 test, 6 kg, 50 cm, (c) S-3 test, 10 kg, 50 cm, and (d) S-4 test, 6 kg, 25 cm.

Table 1. Test conditions.

Test	Dimension (mm)	Explosive Mass (kg)	Explosive Shape	Blast Distance (m)
S-1	125 × 250 × 3000	2	Strip	0.5
S-2	125 × 250 × 3000	6	Strip	0.5
S-3	125 × 250 × 3000	10	Sphere	0.5
S-4	125 × 250 × 3000	6	Sphere	0.25

In the S-1 test, 2 kg of explosives in a strip shape with a length of 50 cm were used. In the S-2 test, 6 kg of explosives were used, formed by bundling three strip-shaped explosives while maintaining a length of 50 cm. In the S-3 test, 10 kg of explosives were used, prepared by cutting five original explosives and packaging them into a spherical shape with a diameter of 22 cm. In the S-4 test, 6 kg of explosives were used, prepared by cutting three original explosives and packaging them into a spherical shape with a diameter of 18.5 cm.

To monitor the changes in overpressure experienced by the reinforced concrete beam during the explosion in real-time, a total of five DFS-50MPa overpressure sensors were installed at the initial position of the beam ends, spaced at intervals of 300 mm. These sensors, characterized by high sensitivity, high precision, and rapid response, accurately captured and recorded the pressure variations of the shock waves generated by the explosion. The schematic layout of the overpressure sensors is shown in Figure 5, while the on-site arrangement is illustrated in Figure 6. After installing the sensors, the calibration began by recording the output signal under zero pressure (0 MPa) and adjusting the initial zero point of the data acquisition system. A standard pressure source was then used to incrementally apply pressure at specified points (e.g., 5 MPa, 10 MPa, 15 MPa). Finally, the pressure was gradually unloaded following the same pressure points in reverse order. Throughout the process, the sensor's output signals were verified to ensure the symmetry and linearity of the data.

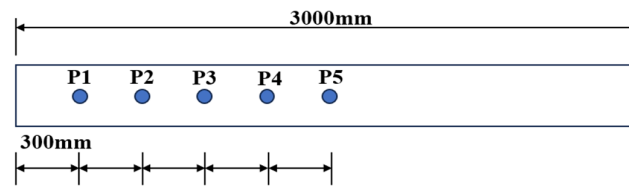


Figure 5. Overpressure sensor arrangement diagram.

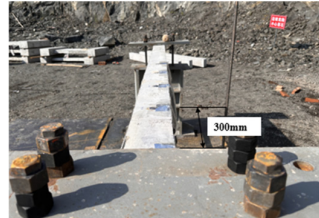


Figure 6. On-site overpressure sensor arrangement diagram.

2.2. Experimental Results

The overall damage condition of the beams during the test is shown in Figure 7, and the localized damage on the blast-facing surface is illustrated in Figure 8.

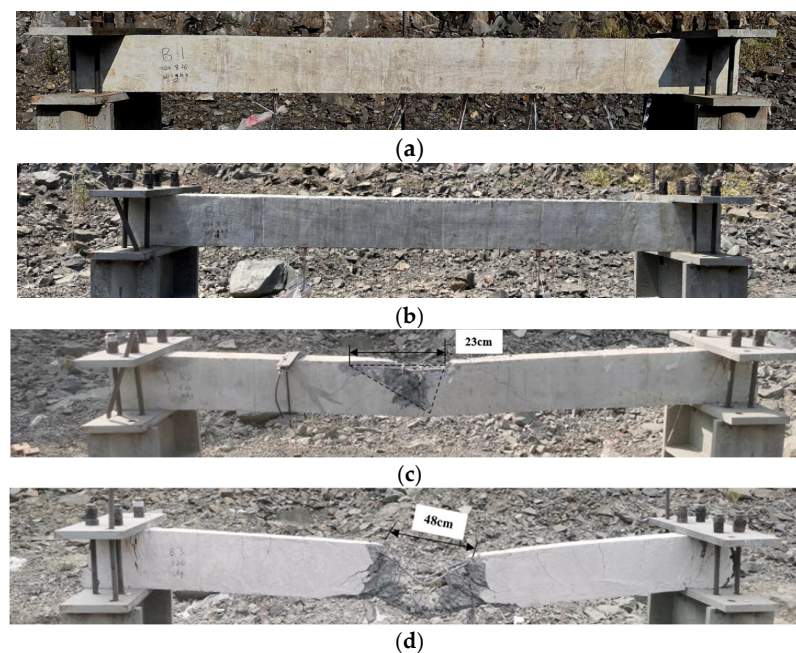


Figure 7. Overall damage diagram of the reinforced concrete beam in the (a) S-1 test, 2 kg, 50 cm, (b) S-2 test, 6 kg, 50 cm, (c) S-3 test, 10 kg, 50 cm, and (d) S-4 test, 6 kg, 25 cm.

In the S-1 test, due to the relatively small explosive equivalent and greater standoff distance, only several small craters were formed on the surface of the reinforced concrete beam, with diameters of approximately 1 mm. The depth of these craters ranged from 0.6 mm to 1.2 mm, indicating minimal surface damage. The craters were distributed sparsely across the beam's surface, with no significant degradation of the beam's structural integrity, as shown in Figure 8a. Although these small craters appeared on the surface, the overall structure of the beam remained intact without cracks or any other form of damage. This indicates that, under conditions of low explosive equivalent and larger standoff distances, the damage caused by the explosion to the reinforced concrete beam is minimal.

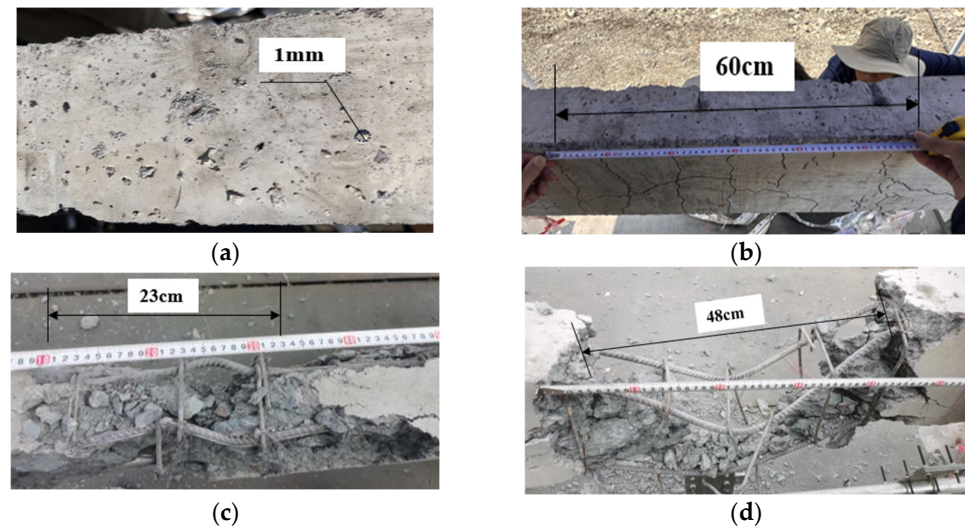


Figure 8. Local damage diagram of the blast-facing surface in the (a) S-1 test, 2 kg, 50 cm, (b) S-2 test, 6 kg, 50 cm, (c) S-3 test, 10 kg, 50 cm, (d) S-4 test, 6 kg, 25 cm.

In the S-2 test, while the shock waves caused by the explosion had some effect on the beam, no significant displacement or large-scale deformation of the beam was observed, as shown in Figure 7b. The beam showed no evident tilting or bending after the explosion, indicating that the structure was not subjected to severe displacement damage. However, in the middle region of the beam, approximately 60 cm from both sides, numerous fine cracks were observed. These cracks were primarily distributed vertically, with some inclined cracks also present. Although these cracks suggest a slight stress concentration on the structure, there was no significant spalling or fragmentation of the concrete, as shown in Figure 8b. Overall, the structure of the beam remained relatively intact, with only minor surface-level damage and no notable functional failure.

In the S-3 test, the damage to the beam was significantly aggravated. The craters on the blast-facing surface became larger, with a fragmentation zone width of 23 cm, as shown in Figure 8c. The longitudinal reinforcement in this region also exhibited substantial deformation, adversely affecting the beam's load resistance. The shock waves not only damaged the surface of the beam, but also caused massive spalling of the concrete on the sides, with the length of the spalled area being approximately 50 cm. Some of the reinforcement bars were exposed, showing significant bending or twisting deformations, indicating that the structure suffered considerable damage from the explosion. Moreover, the maximum mid-span displacement of the beam reached 5 cm, as shown in Figure 7c, suggesting that the structure underwent notable deformation, with some load-bearing functionality already impaired.

In the S-4 test, using 6 kg of spherical No. 2 rock emulsion explosive at a standoff distance of 25 cm, the resulting shock waves were highly powerful, leading to severe bending, fracturing, and collapse of the beam. From a distance, the beam appeared to have broken into two parts. The collapsed and fragmented zone on the rear blast-facing surface connected with the crushed zone on the front blast-facing surface, penetrating the entire structure of the beam. In the middle section of the beam, approximately 48 cm in length, the concrete was completely destroyed, leaving only fine debris, indicating that the structural strength in this area was entirely lost. The reinforcement in this area was completely exposed and exhibited significant deformation, as shown in Figures 7d and 8d. These results demonstrate that, under intense explosive shock waves, the structural strength and stability of the reinforced concrete beam were severely compromised, showing clear structural failure. Under these test conditions, the blast resistance of the entire beam was essentially lost.

By analyzing the results of the test groups, it is evident that, as the explosive equivalent and standoff distance increased, the damage to the reinforced concrete beam intensified significantly. Particularly in the S-3 and S-4 tests, the beams exhibited notable structural damage and even structural failure. This indicates that the explosive equivalent and distance have a significant impact on the damage effect on the beam, and, under high-power explosion conditions, the blast resistance of reinforced concrete beams faces significant challenges.

3. Simulation and Validation

3.1. Numerical Model and Material Parameters

Using the explicit nonlinear FE analysis software LS-DYNA (version [2021]), a three-dimensional numerical model was established to study the dynamic response and damage characteristics of concrete. The FE model is shown in Figure 9. The model consisted of concrete, reinforcement, air domain, clamps, supports, steel bars, and explosives. The numerical simulation employed full-scale modeling with beam dimensions of 250 mm in height, 3000 mm in length, and 125 mm in width. The air domain measured 1500 mm in height, 4000 mm in length, and 400 mm in width. The reinforcement was connected via shared nodes, assuming a fully bonded condition with no slippage. Boundary conditions were set using upper and lower steel plates in the beam support region, with all displacements at the supports fixed.

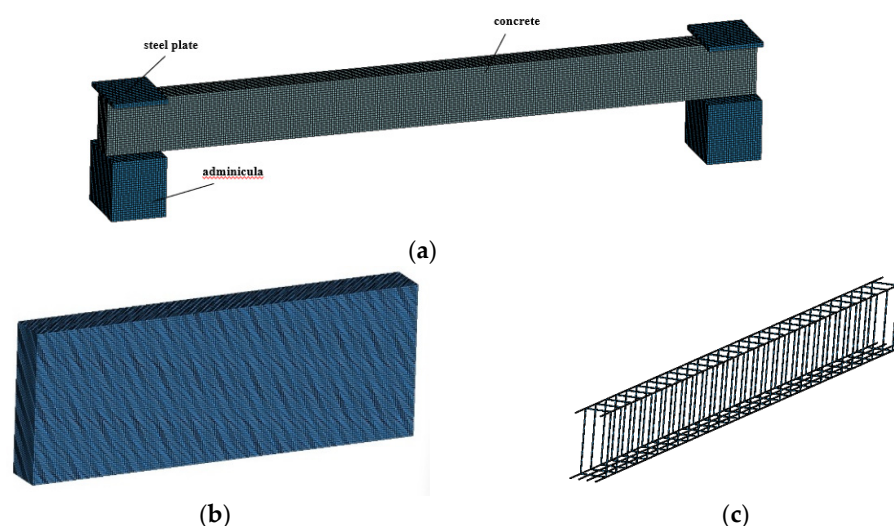


Figure 9. Finite element models: (a) FE model of the concrete beam and supports, (b) FE model of the air domain, and (c) FE model of the reinforcement.

The concrete, reinforcement, air domain, clamps, supports, and explosives were modeled using Solid164 elements, while the reinforcement bars were modeled using Beam161 elements. The air domain mesh was discretized using a Eulerian grid, while the other components were modeled using a Lagrangian grid. A fluid–solid coupling algorithm was applied. Eight-node solid elements were used for modeling concrete, the air domain, clamps, and supports, while two-node beam elements were used for the reinforcement.

Based on the results of the S-4 experiment, four different element sizes were analyzed to determine the optimal mesh size for the numerical model. As shown in Figure 10, five mesh sizes were tested for the concrete and reinforcement elements: 10 mm, 8 mm, 5 mm, and 2 mm. The air domain mesh size was set to twice the concrete element size, and the platen and support mesh sizes were set to four times the concrete element size. The results demonstrate that the 5 mm mesh achieved high accuracy, with the calculated mid-span maximum residual displacement of 10.6 cm closely aligning with the experimental

result of 11.0 cm, yielding an error of 3.6%. Although reducing the mesh size to 2 mm produced comparable accuracy, it significantly increased computational resource demands. Considering both numerical accuracy and computational cost, the optimal mesh sizes were determined as 5 mm for concrete and reinforcement elements, 10 mm for the air domain, and 20 mm for the platen and support elements.

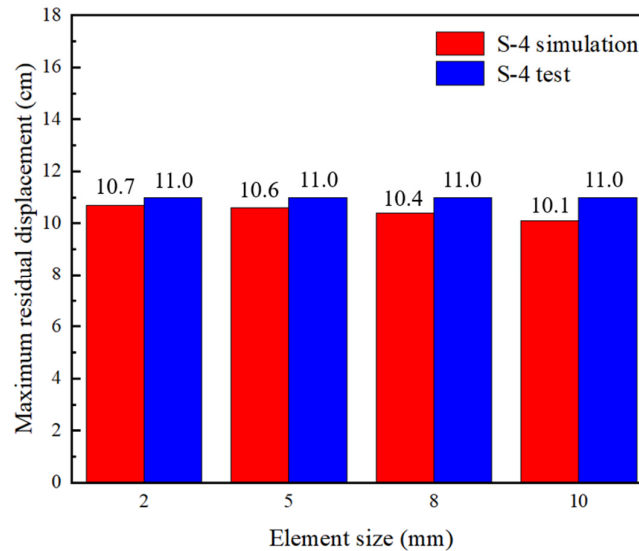


Figure 10. Effect of element size on maximum residual displacement.

The explosive dimensions and position were defined near the center of the air domain's top region using the INITIAL_VOLUME_FRACTION_GEOMETRY keyword. A TNT equivalent was used to model the explosives. Since No. 2 rock emulsion explosive [14] was used in the experiments, its equivalent pressure was scaled by a coefficient of 0.7 to convert the rock emulsion explosive into TNT equivalent for numerical simulation [15,16]. The explosive model was selected as *MAT_HIGH_EXPLOSIVE_BURN, and the equation of state was chosen as *EOS_JWL. The parameters for TNT explosives are listed in Table 2. The CONTACT_AUTOMATIC_SURFACE_TO_SURFACE command was used to model the bonded contact conditions between the concrete and the reinforcement.

Table 2. TNT material parameters.

ρ /(kg·m ⁻³)	D (m·s ⁻¹)	P _{CJ} /GPa	A/GPa	B/GPa	R ₁	R ₂	ω	E ₀ (KJ·m ⁻³)
1630	6930	21	371.3	3.231	4.15	0.95	0.3	7×10^6

To accurately simulate the dynamic response of materials under explosive loading, material models suitable for high strain rate conditions were selected for modeling concrete and reinforcement. The concrete was modeled using the strain-rate-sensitive material model MAT_RHT [17–19]. This model captures the strength enhancement effect and damage characteristics of concrete under high strain rate conditions, with its parameters listed in Table 3. The reinforcement was modeled using the plastic kinematic material model MAT_PLASTIC_KINEMATIC [20] to describe its nonlinear hardening behavior and yield characteristics under dynamic loads, with relevant parameters detailed in Tables 4 and 5 where ρ represents the density of the rebar material, E denotes the Young's modulus, σ indicates the yield strength of the rebar, d refers to the diameter of the rebar, and ν represents the Poisson's ratio. The *MAT_NULL material model was utilized for air, while the equation of state was defined using the ideal gas equation of state, *EOS_LINEAR_PERMUTATION. The material parameters for air are shown in Table 6, ensuring that the propagation properties of the air domain accurately reflect the blast wave propagation process [21].

Table 3. Concrete material parameters.

$\rho/(\text{kg}\cdot\text{m}^{-3})$	f_c/MPa	ν	E/GPa
2500	40	0.2	32.5

Table 4. HRB335 rebar material parameters.

$\rho/(\text{kg}\cdot\text{m}^{-3})$	E/GPa	σ/MPa	d/mm	ν
7800	200	300	6	0.3

Table 5. HRB400 rebar material parameters.

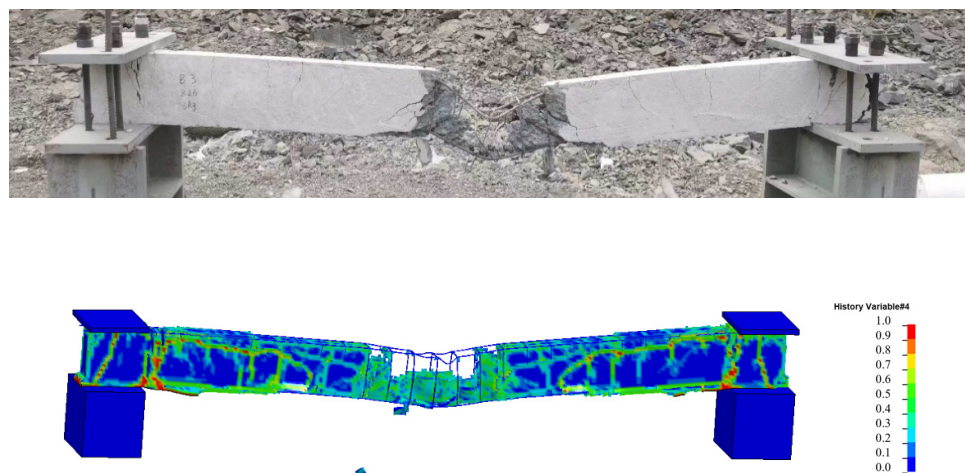
$\rho/(\text{kg}\cdot\text{m}^{-3})$	E/GPa	σ/MPa	d/mm	ν
7800	200	360	10	0.3

Table 6. Air material parameters.

$\rho/(\text{kg}\cdot\text{m}^{-3})$	C_0	C_1	C_2	C_3	C_4	C_5	C_6	$E_0 (\text{KJ}\cdot\text{m}^{-3})$
1.29	0	0	0	0	0.4	0.4	0	253

3.2. Comparison and Analysis of Tests and Simulations

In the S-4 test, the damage morphology of the reinforced concrete beam under explosive shock loading is shown in Figure 11. This test used 6 kg of spherical No. 2 rock emulsion explosive, detonated at a standoff distance of 25 cm. The experimental results revealed severe bending fractures and collapse of the reinforced concrete beam. The collapsed and fragmented region on the rear blast-facing surface connected with the crushed region on the front blast-facing surface, penetrating through the entire beam. Particularly in the middle damage zone, the concrete was almost completely shattered and spalled, leaving only fine rubble. The crater width reached 48 cm, and the maximum residual mid-span displacement of the beam was 11 cm, as shown in Figure 12. The structural strength and stability of the reinforced concrete beam were severely compromised, resulting in significant structural failure.

**Figure 11.** Comparison of the overall damage modes.

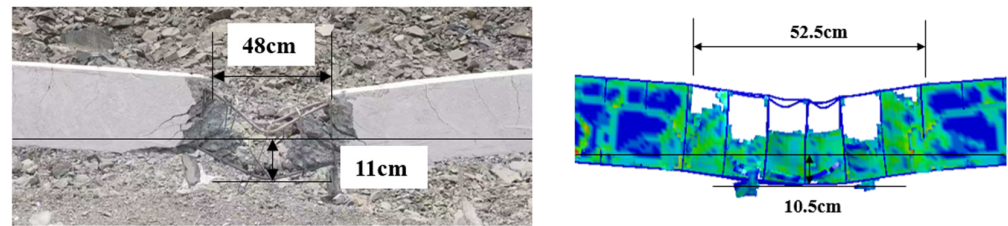


Figure 12. Comparison of local damage dimensions.

The subsequent numerical simulation analysis produced the post-blast damage state of the RC beam which was compared with the experimental results. The failure patterns observed in the simulation were highly consistent with those in the actual experiment, showing a high degree of similarity in the overall damage morphology. Specifically, the beam in the numerical simulation exhibited similar bending fractures and collapse phenomena, with the damage region connecting the rear and front blast-facing surfaces and penetrating through the structure. The crater width obtained from the simulation closely matched the experimental results. In the numerical simulation, the maximum residual displacement reached 10.5 cm, slightly lower than the experimental result of 11 cm, yielding a relative percentage error of approximately 4.5%. Despite this small discrepancy, the results still affirmed the accuracy and reliability of the numerical simulation method in predicting and assessing structural damage.

Additionally, the crater width measured in the simulation was 52.5 cm, which is very close to the experimental result of 48 cm, yielding a relative percentage error of approximately 9.4%. This agreement is visually illustrated in Figure 12. The numerical simulation effectively reproduced the damage modes and extent of destruction of the reinforced concrete beam under explosive loading, with the simulation results being highly consistent with the experimental data. This demonstrates that the adopted numerical calculation model can accurately describe the actual damage behavior of RC beams subjected to explosive loading.

In the S-1 test, due to the explosion point being located near the mid-span of the reinforced concrete beam, the amplitude of the shock wave generated by the explosion was excessively strong. As a result, only the overpressure data from sensors P1 and P2 could be successfully collected during the experiment. This phenomenon was primarily due to the extremely high amplitude of the shock wave at that location, which may have caused the overpressure sensors at other positions to fail in effectively recording the overpressure data under excessive loading.

Nevertheless, by comparing and analyzing the collected overpressure data from the experiment with the peak overpressure values and the rising and falling trends of the overpressure time-history curves obtained from the numerical simulation, a consistent pattern and trend between the two were observed, as shown in Figure 13. This further validates the effectiveness and accuracy of the numerical simulation method in predicting the overpressure effects of explosive shock waves on structures. Additionally, the numerical simulation not only reflects the overpressure response in localized areas, but also provides a reasonable extrapolation of the overall overpressure condition of the beam to a certain extent.

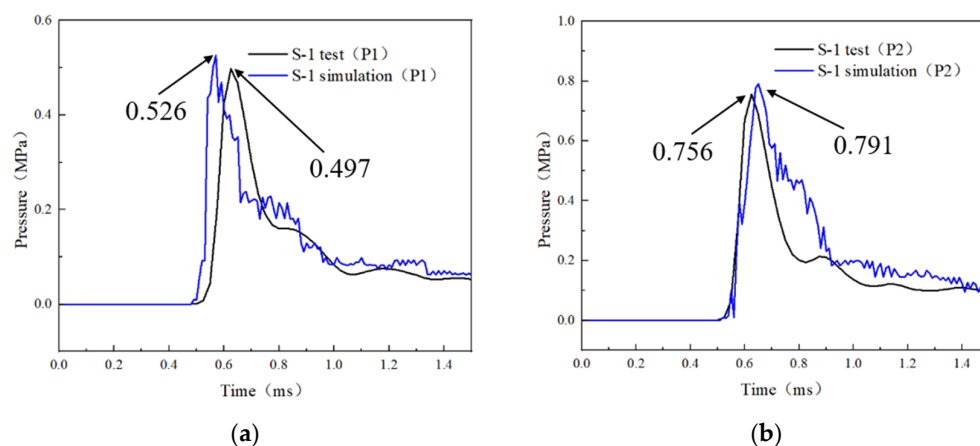


Figure 13. Experimental and numerical simulation overpressure time-history curves from the (a) S-1 test P1 and (b) S-1 test P2.

4. Dynamic Response Analysis

4.1. Simulation Condition Analysis

To further investigate the specific effects of explosive equivalent, standoff distance, and explosive shape on the damage to reinforced concrete beams, 14 LS-DYNA numerical simulation groups were designed. These simulations included explosive equivalents of 2 kg, 4 kg, 6 kg, and 10 kg, standoff distances of 50 cm and 25 cm, and two explosive shapes (spherical and cuboid). The simulation grouping is detailed in Table 7. The amendatory scale distance X is referenced later in the damage criteria section.

Table 7. Grouping of numerical simulations for explosions.

Test	Explosive Mass/kg	Explosive Shape	Blast Distance/m	Scale Distance $Z/(m/kg^{1/3})$	Amendatory Scale Distance $X/(m/kg^{1/3})$
M-1	2	Sphere	0.5	0.629	0.629
M-2	2	Cuboid	0.5	0.629	0.5
M-3	2	Sphere	0.25	0.5	0.5
M-4	2	Cuboid	0.25	0.5	0.4
M-5	4	Sphere	0.5	0.5	0.5
M-6	4	Cuboid	0.5	0.5	0.4
M-7	4	Sphere	0.25	0.396	0.396
M-8	4	Cuboid	0.25	0.396	0.3168
M-9	6	Sphere	0.5	0.436	0.436
M-10	6	Cuboid	0.5	0.436	0.348
M-11	6	Sphere	0.25	0.346	0.346
M-12	6	Cuboid	0.25	0.346	0.2768
M-13	10	Sphere	0.5	0.368	0.368
M-14	10	Cuboid	0.5	0.368	0.294

Under a standoff distance of 50 cm, when using 2 kg of spherical explosives for explosion testing, the damage to the reinforced concrete beam was relatively minor, with only a few cracks observed, and the overall structure remained intact, as shown in Figure 14a. In comparison, for simulation M-2 (Figure 14b), which used the same equivalent weight but a cuboid explosive, the damage degree was similar to that caused by the spherical explosive, but the crack propagation was slightly more noticeable. This suggests that cuboid explosives may generate more concentrated destructive effects in certain directions.

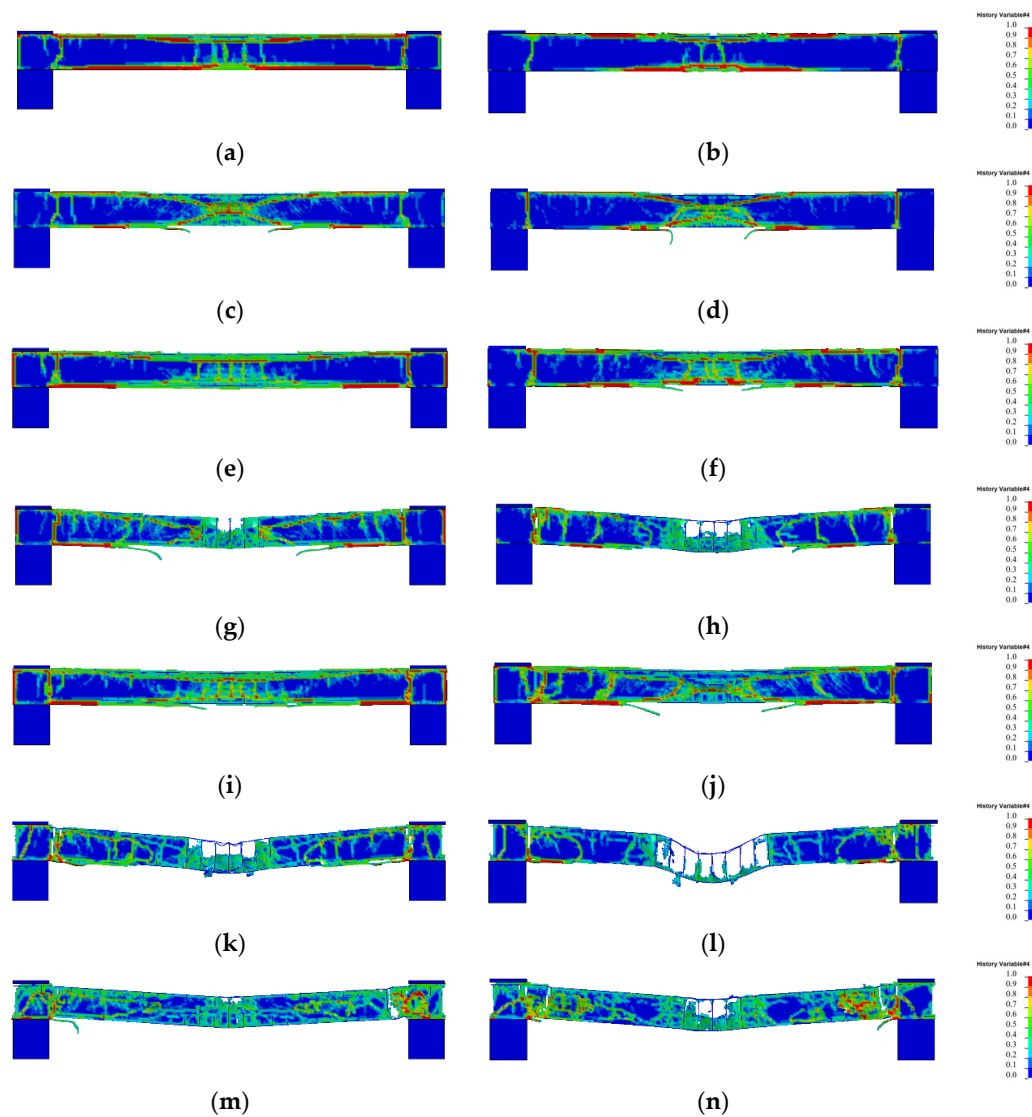


Figure 14. Numerical simulation damage diagrams FOR (a) M-1, 2 kg, 50 cm, sphere, (b) M-2, 2 kg, 50 cm, cuboid, (c) M-3, 2 kg, 25 cm sphere, (d) M-4, 2 kg, 25 cm, cuboid, (e) M-5, 4 kg, 50 cm, sphere, (f) M-6, 4 kg, 50 cm, cuboid, (g) M-7, 4 kg, 25 cm, sphere, (h) M-8, 4 kg, 25 cm, cuboid, (i) M-9, 6 kg, 50 cm, sphere, (j) M-10, 6 kg, 50 cm, cuboid, (k) M-11, 6 kg, 25 cm, sphere, (l) M-12, 6 kg, 25 cm, cuboid, (m) M-13, 10 kg, 50 cm sphere, and (n) M-14, 10 kg, 50 cm, cuboid.

When the explosive equivalent was increased to 4 kg, the spherical explosives caused more cracks on the beam, with the damage degree increasing, though the depth and range of these cracks remained limited, as shown in Figure 14e. However, under the same equivalent weight of cuboid explosives, the cracks became significantly more pronounced, especially near the explosion center, where the damaged area notably expanded. This indicates that cuboid explosives exert stronger localized destructive forces, as shown in Figure 14f.

As the explosive equivalent was further increased to 6 kg (Figure 14i), the spherical explosives led to more severe cracking, and the beam's localized damage increased significantly, compromising structural integrity. Under the effect of 6 kg of cuboid explosives, the damage area expanded further, and the overall stability of the beam significantly declined, demonstrating that cuboid explosives cause more severe structural damage at higher equivalents.

When the explosive equivalent reached 10 kg, the spherical explosives caused widespread cracking and damage to the beam structure, with cracks almost penetrating the

entire thickness of the beam. Under the same equivalent weight of cuboid explosives, the damage was more catastrophic, severely compromising the structural integrity of the beam. The beam exhibited extensive damage, approaching a state of near fracture, as shown in Figure 14n. This further proves that cuboid explosives have a more pronounced destructive effect on structures at higher equivalents.

When the standoff distance was reduced to 25 cm, both spherical and cuboid explosives caused significantly enhanced damage to the reinforced concrete beam. Under 2 kg of spherical explosives, the beam showed noticeable cracks, and the damaged area increased, though the overall structure retained some integrity. However, with the same weight of cuboid explosives, the damage degree was slightly higher than that of spherical explosives, with more extensive cracking. This indicates that, at smaller standoff distances, cuboid explosives exhibit a stronger destructive effect.

When the explosive equivalent was increased to 4 kg, spherical explosives further expanded the cracks on the beam, increasing the damaged area, with noticeable localized structural damage, as shown in Figure 14h. Under the effect of cuboid explosives, the depth and range of the cracks significantly increased, with the overall structure suffering greater damage and the destruction becoming more pronounced.

In simulations with 6 kg of explosives, the spherical explosives caused widespread cracking and damage to the beam, significantly reducing its integrity and making the structure more fragile. Under the effect of cuboid explosives, the damage reached its peak, with the beam structure almost completely fractured. Cracks penetrated the core of the beam, and the damaged area was extensive, as shown in Figure 14l. These observations further confirm that reducing the standoff distance significantly amplifies the impact of explosions on structures. Moreover, they highlight the critical influence of explosive shape on the propagation and destructive effects of blast waves.

To further understand the differences in the destructive effects of cuboid and spherical explosives, an energy dissipation analysis can shed light on the variations in shock wave propagation. Cuboid explosives, with their extended shape, disperse energy over a larger area, resulting in more widespread cracking. In contrast, spherical explosives focus energy into a more concentrated blast, causing localized damage with less energy loss. This disparity in energy distribution is a key factor in the differing damage patterns, with cuboid explosives generally inflicting more structural damage at the same equivalent weight.

In summary, at smaller standoff distances, the destructive effects of explosives significantly intensify. Cuboid explosives generally cause greater damage to reinforced concrete beams compared to spherical explosives at the same equivalent weight. As the explosive equivalent increases, the degree of damage to the beam increases significantly, regardless of the shape of the explosive.

4.2. Parameter Analysis

4.2.1. Maximum Residual Displacement

Figure 15 illustrates the variation trends of the maximum residual displacement of reinforced concrete beams under different standoff distances and explosive shapes as a function of explosive equivalent, shape, and distance. The data show that the maximum residual displacement at a standoff distance of 25 cm was generally higher than that under the 50 cm condition. Specifically, at a shorter standoff distance, the shock and pressure waves generated by the explosion acted more directly and intensely on the target structure, resulting in greater residual displacement.

A comparison of the effects of different explosive shapes reveals that the maximum residual displacement caused by the cuboid explosives at a standoff distance of 25 cm was significantly higher than that under other conditions. This phenomenon indicates that, due

to their geometric characteristics, cuboid explosives release more concentrated and intense shock waves during the explosion, exerting greater impact loads on the target structure and leading to larger displacement deformation. This effect became more pronounced as the explosive equivalent increased, with the maximum residual displacement exhibiting a rapid growth trend. The more concentrated and intense shock waves from the cuboid explosives resulted in prolonged oscillations within the structure, with energy dissipation occurring more slowly. This extended oscillation time led to greater displacement compared to the more focused energy release of the spherical explosives.

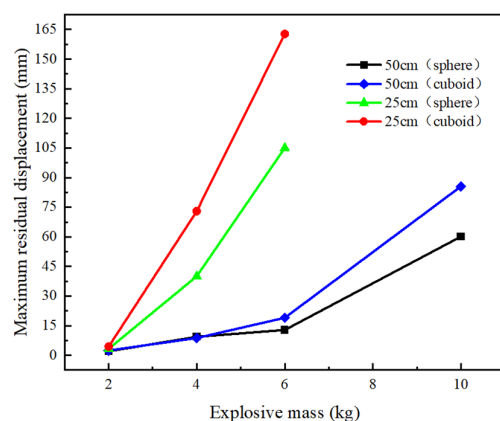


Figure 15. Maximum residual displacement of the beam.

In contrast, while the spherical explosives also caused significantly higher residual displacement at a standoff distance of 25 cm compared to 50 cm, the growth rate was slightly lower than that of cuboid explosives. This difference can be attributed to the more uniform and dispersed shock wave distribution produced by spherical explosives during detonation, resulting in a relatively weaker localized impact on the target structure. However, under the 50 cm standoff condition, the growth trends of the residual displacement for both spherical and cuboid explosives became similar as the explosive equivalent increased. This is primarily because, at larger standoff distances, the differences in shock wave intensity and pressure distribution between the two shapes diminish significantly after propagating over a similar distance, leading to a comparable impact on the structure.

In summary, standoff distance and explosive shape have significant effects on structural residual displacement. A smaller standoff distance (25 cm) significantly enhances the intensity and effectiveness of explosive shock waves, resulting in greater residual displacement. Furthermore, cuboid explosives, due to their more concentrated shock wave characteristics, exhibit more pronounced destructive effects under smaller standoff distances, particularly at higher explosive equivalents. This shape-specific characteristic underscores their greater structural damage potential.

4.2.2. Crater Depth

Figure 16 illustrates the variation trends of crater depth in reinforced concrete beams under different explosive equivalents, standoff distances, and explosive shapes. From the figure, it is obvious that the crater depth was significantly greater at shorter standoff distances (25 cm) compared to longer distances (50 cm), directly revealing the close relationship between standoff distance and explosive effects. Specifically, at shorter standoff distances, the energy released by the explosion acted more intensely and directly on the surface of the target structure. This concentrated impact of shock and pressure waves resulted in a significant increase in crater depth. In contrast, at a standoff distance of 50 cm,

the energy density acting on the beam surface was relatively lower due to the attenuation of explosive shock waves during propagation, leading to shallower craters.

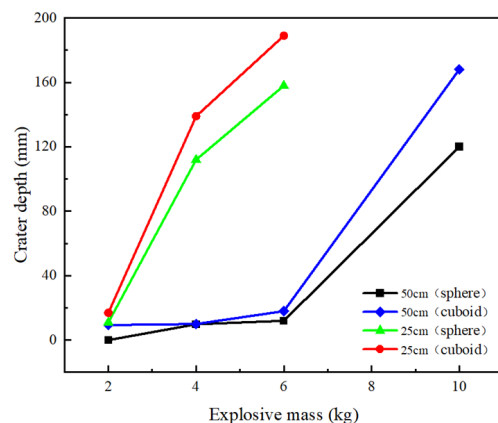


Figure 16. Depth of explosion crater on the beam.

Under the same standoff distance, comparing the crater depths produced by cuboid and spherical explosives reveals that cuboid explosives tended to create deeper craters in the experiments. This phenomenon is primarily attributed to the influence that explosive shape exerts on the propagation characteristics of shock waves. The shape of cuboid explosives causes the energy released during the explosion to be more concentrated in specific directions, resulting in deeper localized damage on the target structure. Conversely, spherical explosives, due to their uniform shape, produce more evenly distributed shock waves in all directions. While their overall damage range is more uniform, the concentrated energy acting on a localized area is relatively lower, resulting in shallower craters.

The influence of explosive equivalent is also clearly depicted in the figure. As the explosive equivalent increased, the growth trend of crater depth became particularly significant. This is because, with higher explosive equivalents, the total energy released by the explosion increases, significantly enhancing the intensity and pressure amplitude of the shock waves. Consequently, the destructive load applied to the beam surface is greater, leading to deeper craters. This trend was especially pronounced at shorter standoff distances (25 cm), indicating that the combination of high explosive equivalent and short standoff distance greatly amplifies localized damage effects on the beam.

Although the findings presented offer valuable insights into the impact of standoff distance, explosive shape, and explosive equivalent on crater depth, it is essential to recognize that real-world explosion conditions may be influenced by additional factors such as air resistance and terrain irregularities. These external factors could alter shock wave propagation and energy dissipation, effects not accounted for in the current simulations. For example, variations in terrain may lead to changes in how shock waves are distributed across the target, potentially modifying both crater depth and overall damage patterns. Additionally, air resistance could reduce the intensity of shock waves over greater distances, especially in open or outdoor environments. Future research could consider integrating these variables to better understand blast effects in more complex, real-world scenarios.

In summary, standoff distance, explosive shape, and explosive equivalent are critical factors in determining crater depth. Shorter standoff distances (25 cm) significantly enhance the localized effects of explosions, resulting in deeper craters. Additionally, due to their shape characteristics, cuboid explosives generate more concentrated shock waves during detonation, thereby creating deeper craters under the same conditions. As the explosive equivalent increases, this difference becomes more pronounced, with crater depth showing a rapid growth trend.

4.2.3. Time-History Displacement

Figure 17 demonstrates that the standoff distance significantly affects the damage degree of reinforced concrete beams. When the standoff distance is small, the energy released by the explosion acts intensely on the beam within a very short time, resulting in relatively large displacements. Due to the short propagation distance, the energy loss during propagation is minimal, allowing the explosion wave to quickly and forcefully deform the beam. In this case, oscillation phenomena in the beam are not evident because the energy released by the explosion is almost directly absorbed by the beam and rapidly converted into displacement, without sufficient time to form complex internal wave reflections or oscillations, thus significantly reducing the oscillation effects.

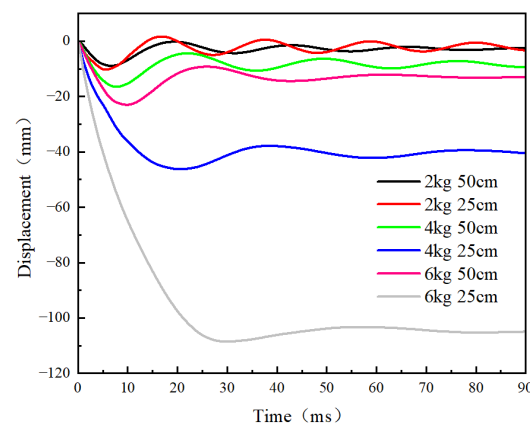


Figure 17. Displacement time-history curves of explosives under different charges and standoff distances.

Furthermore, at smaller standoff distances, the impact of reflected shock waves on displacement becomes a critical factor. As the initial shock wave interacts with the surface of the beam, a portion of the wave reflects back and interacts with subsequent waves, amplifying the localized forces acting on the structure. This phenomenon can contribute to the rapid and intense deformation of the beam, compounding the effects of the direct explosion wave. These reflected waves also influence the directionality of displacement, further intensifying the damage in certain regions.

Conversely, when the standoff distance increases, the explosion wave experiences energy dissipation due to air resistance and other mechanisms during propagation, leading to a significant reduction in the energy reaching the beam surface. This directly results in a sharp decrease in the displacement of the beam. Additionally, under larger standoff distances, the interaction between the explosion wave and the beam generates more reflection and scattering phenomena. These wave interactions create complex oscillation patterns within the beam which not only affect its deformation, but also alter the distribution characteristics of its displacement.

As indicated in Figure 17, as the explosive equivalent increased, the impact force generated by the explosion increased significantly. This is because an increase in explosive equivalent directly raises the total energy released by the explosion, thereby significantly enhancing the intensity of the explosion wave and its impact on the target structure. Under these conditions, the beam is subjected to greater external forces, leading to a notable increase in displacement. Additionally, with the enhancement of impact forces, the time-history curves of the beam exhibit higher peak accelerations and displacements. This phenomenon can be explained by the fact that stronger impact forces cause the beam to accelerate deformation over a very short time, resulting in higher peak features on the time-history curves.

The influence of explosive shape is also visually reflected in the figures. Due to their geometric properties, cuboid explosives release more concentrated energy during detonation. This energy concentration effect enables cuboid explosives to more effectively deform reinforced concrete beams under conditions of shorter standoff distances and higher explosive equivalents, leading to greater displacements, as shown in Figure 18. In contrast, spherical explosives, with their uniform shape, produce explosion waves that propagate more evenly in all directions, resulting in greater energy dispersion. Consequently, the energy acting on the localized target structure is lower, leading to relatively smaller displacements.

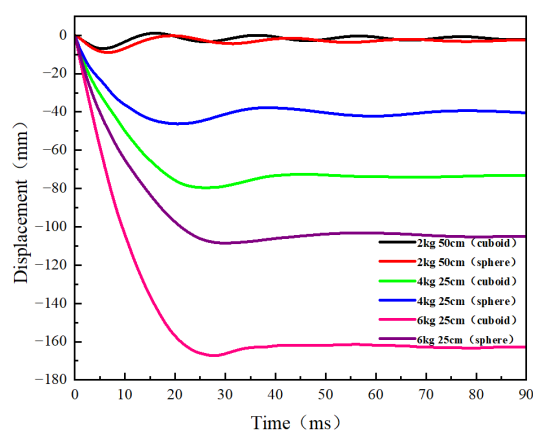


Figure 18. Displacement time-history curves under different explosive shapes.

In conclusion, standoff distance, explosive equivalent, and explosive shape significantly influence the displacement and damage characteristics of reinforced concrete beams. Shorter standoff distances and the concentrated energy release properties of cuboid explosives play a critical role in increasing displacements. Additionally, the increase in explosive equivalent further amplifies the explosion impact effects, causing the beam to experience greater deformation and displacement over a shorter period.

These findings on displacement trends have important implications for building design and blast resistance. The relationship between standoff distance, explosive equivalent, and displacement underscores the need for structures to withstand both localized and distributed blast effects. In urban areas where explosions may occur at shorter standoff distances, reinforced concrete beams and other components must be designed to absorb higher concentrated energy, possibly through reinforcement strategies that enhance ductility and energy dissipation.

For structures exposed to longer standoff distances, design considerations should account for more complex shock wave propagation, including oscillation damping to mitigate reflected and scattered waves. Features like shock-absorbing materials and designs that allow controlled deformation could help reduce energy transmission. Additionally, understanding the impact of explosive shape on energy distribution highlights the importance of optimizing structural geometry for better blast resistance.

Incorporating these insights into building design can aid engineers and architects in creating more resilient structures, enhancing safety and infrastructure robustness.

4.2.4. Time-History Overpressure and Impulse

Figure 19 illustrates the time-history overpressure curves generated by explosives under different equivalent conditions. The figure clearly shows that, as the explosive equivalent increased, the peak overpressure exhibited a significant upward trend. Specifically, for lower explosive equivalents, the peak overpressure generated by the explosion was relatively low, and the overpressure decayed rapidly to zero over a short time. However, with

higher explosive equivalents, the peak overpressure rose significantly, and the duration of the overpressure also extended accordingly. This indicates that high-equivalent explosives release a greater total energy, resulting in stronger and more prolonged shock waves, thereby significantly expanding the range of their effects on the surrounding medium. The extended duration of the overpressure further suggests that, as the equivalent increases, the energy dissipation process of the shock wave becomes slower. This phenomenon highlights the critical role of explosive equivalent in determining the intensity and duration of explosion shock waves.

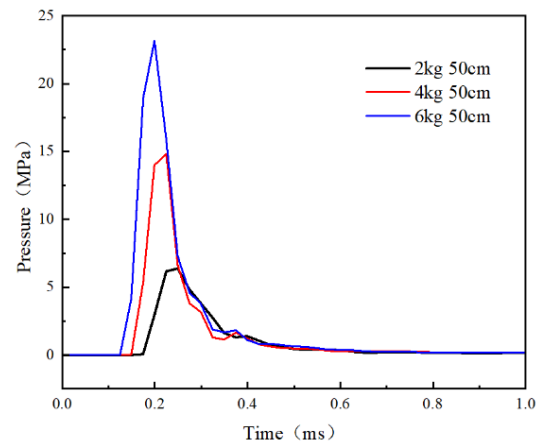


Figure 19. Overpressure time-history curves of explosives under different charges.

Figure 20 further illustrates the time-history impulse curves for spherical explosives under different equivalent conditions. Impulse trends are closely linked to structural failure patterns, as the impulse magnitude reflects the cumulative force exerted on the structure during the explosion shock wave. Higher impulse values indicate exposure to greater peak forces and longer loading durations, increasing the likelihood of failure. This is due to stress concentration and material fatigue from prolonged intense loading. Higher impulses can result in severe cracking, spalling, and fragmentation of concrete, as seen in high-equivalent explosive scenarios. The results indicate a clear positive correlation between impulse and explosive equivalent. The increase in explosive equivalent not only elevated the peak overpressure, but also extended the duration of the overpressure, directly resulting in an increase in impulse. This indicates that the explosion shock waves from high-equivalent explosives exert a greater cumulative force on the target structure over a longer duration, thereby causing more significant damage to the structure.

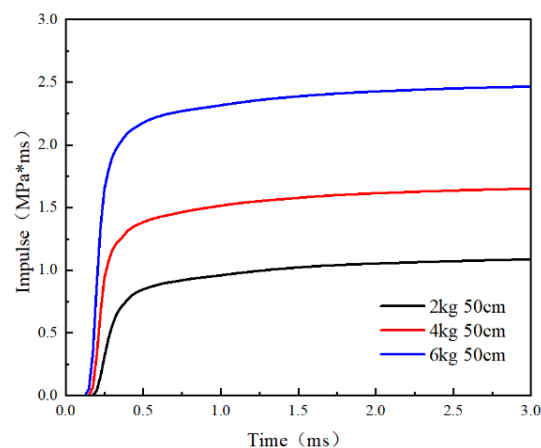


Figure 20. Impulse time-history curves of explosives under different charges.

At a standoff distance of 25 cm, the overpressure was generally higher than that under the 50 cm condition, as shown in Figure 21. A shorter standoff distance resulted in a stronger impact of the explosion on the structure, enabling the overpressure to reach higher peaks more quickly and sustain higher values. As the standoff distance decreased, the impulse also showed an increasing trend.

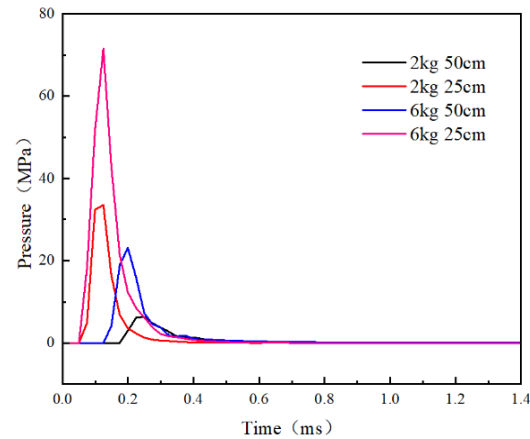


Figure 21. Overpressure time-history curves of explosives under different standoff distances.

The experimental results in Figure 21 indicate that, at a standoff distance of 25 cm, the overpressure generated by the explosive was consistently higher than that at 50 cm. This demonstrates that the standoff distance is a critical factor influencing overpressure intensity and impulse. At shorter standoff distances, the propagation distance of the shock wave is reduced, and the effects of air resistance and other energy dissipation mechanisms are relatively minimal. Consequently, the shock wave acts on the target structure with higher intensity. This not only significantly increases the overpressure peak, but also extends the duration of overpressure, thereby amplifying the destructive effects of the explosion on the target structure.

Additionally, as shown in Figure 22, the impulse generated by the explosive also exhibited a clear increasing trend as the standoff distance decreased. Impulse, being the time-integrated result of overpressure, is influenced not only by the overpressure peak, but also by its duration. Under shorter standoff distance conditions, the higher overpressure peaks and longer durations led to a significant increase in cumulative impulse. This indicates that shorter standoff distances enable the explosion shock wave to act more intensely and in a more focused manner on the target structure, resulting in a greater total force and more pronounced destructive effects.

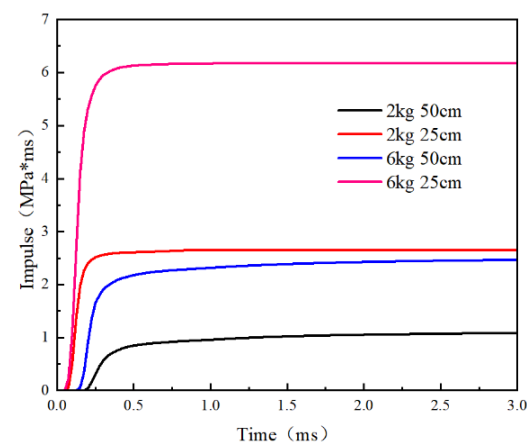


Figure 22. Impulse time-history curves of explosives under different standoff distances.

When comparing the explosion effects of different explosive shapes, Figure 23 shows that the overpressure generated by the cuboid explosives at a standoff distance of 25 cm was particularly significant. As the explosive equivalent increased, the overpressure produced by the cuboid explosives rose sharply, with peak overpressure values being significantly higher than those of the spherical explosives under the same conditions. This indicates that, at shorter standoff distances, the geometric characteristics of cuboid explosives allow them to release energy more effectively, resulting in more intense shock effects.

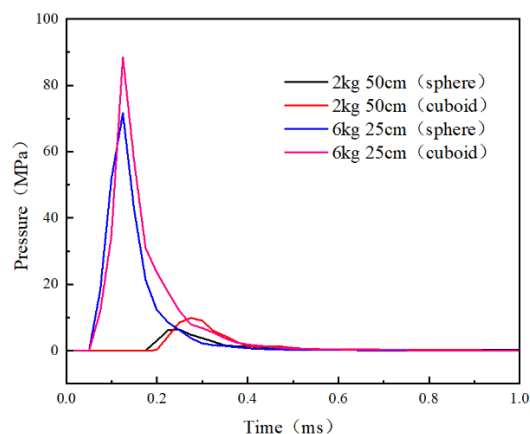


Figure 23. Overpressure time-history curves under different explosive shapes.

This phenomenon can be attributed to the influence of the geometric shape of cuboid explosives on the propagation characteristics of explosion waves. Due to their more directional shape, cuboid explosives release energy more concentratedly in specific directions. This concentration results in stronger shock waves acting on the target structure, leading to a notable increase in peak overpressure. This focused effect is especially evident at shorter standoff distances, where the reduction in shock wave energy over the shorter propagation distance is minimal, allowing it to act more directly and forcefully on the target.

In contrast, the overpressure performance of the spherical explosives was relatively more balanced. Although the spherical explosives also showed an increasing trend in overpressure with higher equivalents, their growth rate at a standoff distance of 25 cm was slightly lower than that of the cuboid explosives. This is because the geometric shape of spherical explosives allows the explosion wave energy to spread uniformly in all directions, reducing the energy density in any particular region. As a result, their peak overpressure is relatively lower. Therefore, under the same standoff distance and equivalent conditions, the shock effect of spherical explosives is less pronounced compared to cuboid explosives.

Structural asymmetry can amplify differences in damage patterns caused by cuboid and spherical explosives. Cuboid explosives, with a directional energy release, may concentrate forces on weaker or irregular areas, leading to uneven damage and localized stress. In contrast, spherical explosives, with a uniform energy dispersion, produce a more balanced impact, minimizing the influence of asymmetry.

The change in explosive shape also significantly affects impulse. As shown in Figure 24, as the explosive shape transitioned from spherical to cuboid, the impulse exhibited a marked increase. This is because the concentrated energy released by cuboid explosives not only results in higher peak overpressure, but also extends the duration of overpressure, leading to a substantial increase in impulse. In contrast, while the spherical explosives also showed an upward trend in impulse with increasing equivalent, their energy release was relatively dispersed, resulting in a lower growth rate of the impulse compared to cuboid explosives.

Comprehensive analysis indicates that explosive equivalent is a critical factor influencing overpressure and impulse. As the explosive equivalent increases, the peak overpressure generated by the explosion rises significantly, the duration of overpressure extends, and, consequently, the impulse also increases. A smaller standoff distance enhances the intensity and focus of the shock wave, resulting in higher peak overpressure, longer overpressure duration, and significantly increased impulse. Cuboid explosives, under conditions of smaller standoff distances (25 cm) and higher equivalents, exhibit more concentrated energy release, generating greater overpressure and impulse and demonstrating stronger shock effects.

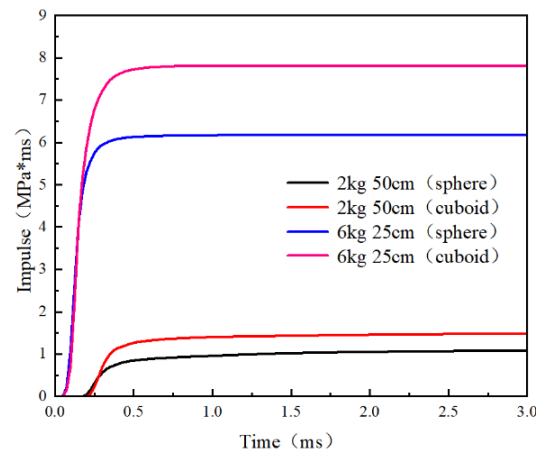


Figure 24. Impulse time-history curves under different explosive shapes.

4.3. Damage Assessment Criteria

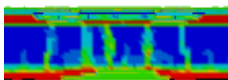
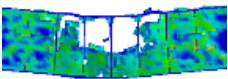
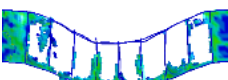
In the in-depth study of near-field explosion effects, the damage assessment criteria for reinforced concrete beams proposed by Wei Wang [13] were referenced. These criteria are based on the scaled standoff distance Z , a key parameter that accounts for the relationship between explosive equivalent and explosion height, providing a quantitative standard for evaluating beam damage levels. When $Z > 0.4 \text{ m/kg}^{1/3}$, the reinforced concrete beam sustains minor damage. On the blast-facing side, minor spalling of the concrete occurs, but the overall structure maintains stability. As Z decreases to the range of $0.3 \text{ m/kg}^{1/3} \leq Z \leq 0.4 \text{ m/kg}^{1/3}$, the damage level escalates to moderate damage, with noticeable spalling of the protective concrete layer on the blast-facing side. Some concrete within the stirrups may be crushed, and bending or fracture of the concrete may appear on the rear blast side. When Z further decreases to $0.28 \text{ m/kg}^{1/3} \leq Z < 0.3 \text{ m/kg}^{1/3}$, the beam suffers severe damage. The top crushed area on the beam forms an inverted triangular cone, with stirrups exposed. Triangular cone-shaped cracks may connect the crushed area to the rear blast side, and minor spalling may appear on the central concrete surface. For $Z < 0.28 \text{ m/kg}^{1/3}$, the beam experiences complete damage, with the midsection undergoing extensive bending and fragmentation, forming a large, crushed area. The top crushed zone also forms an inverted triangular cone, with extensive triangular cone-shaped cracks on the rear blast side. The central concrete surface suffers large-scale spalling, and significant portions of the longitudinal reinforcement are exposed.

The shape of the explosive significantly influences the damage pattern of the beam. It can be observed that, under the M-14 simulation condition, as shown in Figure 14n, the damage to the beam caused by the rectangular explosive clearly falls into the category of severe damage rather than moderate damage. Similarly, in the M-12 simulation condition, as shown in Figure 14l, the damage caused by the rectangular explosive clearly belongs to the category of complete destruction rather than severe damage. This indicates that

the original damage criteria are not rigorous enough. To address this issue, a shape-specific correction factor was introduced into the damage criteria to ensure that the damage assessment for these two conditions falls into the correct damage levels. Specifically, cuboid explosives have a correction factor of 0.8, indicating that their damage effects are slightly weaker compared to spherical explosives (correction factor = 1). This adjustment ensures a more accurate evaluation of damage caused by explosives of different shapes.

Based on the above analysis, the damage levels of reinforced concrete beams under explosive loading were categorized into four grades. Each grade corresponds to a specific range of scaled standoff distances and associated damage characteristics, as summarized in Table 8.

Table 8. Damage criteria.

Damage Levels	Main Characteristics	Adjusted Scaled Standoff Distance
Minor damage 	On the rear blast-facing side of the beam, a few cracks were observed, while small areas of concrete spalling were also noted on both sides of the central region of the top surface.	$X > 0.4$
Moderate damage 	The midsection of the beam experienced significant bending stress, resulting in noticeable crushing damage in this area. Additionally, triangular cone-shaped fracture cracks were observed at other locations on the sides of the beam.	$0.3 < X < 0.4$
Severe damage 	The entire beam underwent significant deformation, with the blast-facing side subjected to severe compressive forces, resulting in a distinct inverted triangular cone-shaped crushed area. In the central region of the rear blast-facing side, minor spalling of the concrete surface was observed.	$0.28 < X < 0.3$
Complete damage 	The beam experienced severe bending and fracturing, ultimately leading to collapse. On the rear blast-facing side, the collapsed and fragmented area connected with the heavily crushed region on the blast-facing side, forming a continuous damage zone through the beam.	$X < 0.28$

5. Conclusions

This study conducted close-range airburst tests on reinforced concrete beams subjected to explosives of different shapes, equivalents, and at different standoff distances, combined with numerical simulations using the LS-DYNA software. The damage characteristics were qualitatively and quantitatively analyzed, and optimized damage assessment criteria were established.

(1) Explosive shape, equivalent, and standoff distance significantly influence the propagation and destructive effects of shock waves on reinforced concrete beams.

(2) Cuboid explosives generate more concentrated shock waves, leading to greater structural damage compared to spherical explosives.

(3) Shorter standoff distances and larger explosive equivalents amplify damage severity, as reflected in residual displacement and crater depth.

(4) The damage modes of reinforced concrete beams were revised according to the corrected scaled standoff distance X under different explosive shapes: minor damage ($X > 0.4 \text{ m/kg}^{1/3}$), a few cracks are observed on the rear blast side, with minor concrete spalling on both sides of the top surface center; moderate damage ($0.3 \text{ m/kg}^{1/3} < X < 0.4 \text{ m/kg}^{1/3}$), noticeable bending and crushing damage appears in the midsection of the beam, with triangular cone-shaped fracture cracks observed on other side regions; severe damage ($0.28 \text{ m/kg}^{1/3} < X < 0.3 \text{ m/kg}^{1/3}$), the beam exhibits significant deformation, with an inverted triangular cone-shaped crushed region on the blast-facing side and minor concrete spalling at the center of the rear blast side; complete

damage ($X < 0.28 \text{ m/kg}^{1/3}$), the beam experiences bending, fracturing, and collapse, with the collapsed and fragmented regions on the rear blast side connecting with the crushed regions on the blast-facing side to form a continuous damage zone.

Strengths of the Model

- (1) Provides accurate predictions of damage severity under various explosive scenarios.
- (2) Establishes revised damage criteria that incorporate shape-specific correction factors for improved assessment accuracy.

Limitations of the Model

- (1) Simplifications of environmental conditions (e.g., no terrain or air resistance effects) may limit real-world applicability.
- (2) The model's applicability to more complex structural geometries (e.g., multi-element or 3D reinforced designs) remains untested.

Design Recommendations

The findings of this study highlight the importance of considering explosive shape, equivalent, and standoff distance in the design of reinforced concrete structures to enhance blast resistance. Specifically, structures exposed to higher blast risks could benefit from:

- (1) Reinforcement strategies such as increasing the ductility and energy dissipation capacity of materials in critical load-bearing elements.
- (2) Introducing structural features that mitigate localized damage effects caused by concentrated blast energy, such as that of cuboid explosives.
- (3) Adopting optimized scaled standoff distance criteria to guide structural designs for improved resilience under explosive loads.

Further Research

- (1) The behavior of reinforced concrete beams under more complex blast environments, including oblique shock angles or multi-explosive scenarios.
- (2) The development of 3D reinforcement models to better predict the behavior of internal steel reinforcements under extreme loads.
- (3) The role of environmental factors, such as terrain irregularities and air resistance, in shock wave propagation and structural damage assessment.

Author Contributions: Formal analysis, Y.M.; Investigation, Y.M., W.L. and S.S.; Writing—original draft, Y.M.; Writing—review & editing, R.Z., W.W. and C.Y. All authors have read and agreed to the published version of the manuscript.

Funding: This research received no external funding.

Data Availability Statement: Data are contained within the article.

Conflicts of Interest: The authors declare no conflict of interest.

References

1. Smith, P.J. Terrorism in Asia: A Persistent Challenge Sustained by Ideological, Physical, and Criminal Enablers. In *Handbook of Asian Criminology*; Liu, J., Heberton, B., Jou, S., Eds.; Springer: New York, NY, USA, 2013; pp. 147–164, ISBN 978-1-4614-5218-8.
2. Shi, Y.; Stewart, M.G. Damage and risk assessment for reinforced concrete wall panels subjected to explosive blast loading. *Int. J. Impact Eng.* **2015**, *85*, 5–19. [[CrossRef](#)]
3. Shi, Y.; Xiong, W.; Li, Z.-X.; Xu, Q. Experimental studies on the local damage and fragments of unreinforced masonry walls under close-in explosions. *Int. J. Impact Eng.* **2016**, *90*, 122–131. [[CrossRef](#)]
4. Dua, A.; Braimah, A.; Kumar, M. Experimental and numerical investigation of rectangular reinforced concrete columns under contact explosion effects. *Eng. Struct.* **2020**, *205*, 109891. [[CrossRef](#)]
5. Luccioni, B.M.; Ambrosini, R.D.; Danesi, R.F. Analysis of building collapse under blast loads. *Eng. Struct.* **2004**, *26*, 63–71. [[CrossRef](#)]

6. Osteraas, J.D. Murrah building bombing revisited: A qualitative assessment of blast damage and collapse patterns. *J. Perform. Constr. Facil.* **2006**, *20*, 330–335. [[CrossRef](#)]
7. Wang, W. Mechanical Research on Reinforced Concrete Materials. *Materials* **2023**, *16*, 6892. [[CrossRef](#)] [[PubMed](#)]
8. Shafighfar, T.; Kazemi, F.; Bagherzadeh, F.; Mieloszyk, M.; Yoo, D. Chained machine learning model for predicting load capacity and ductility of steel fiber-reinforced concrete beams. *Comput. Aided Civ. Eng.* **2024**, *39*, 3573–3594. [[CrossRef](#)]
9. Zhang, C.; Gholipour, G.; Mousavi, A.A. Blast loads induced responses of RC structural members: State-of-the-art review. *Compos. Part B Eng.* **2020**, *195*, 108066. [[CrossRef](#)]
10. Yang, C.; Jia, X.; Huang, Z.; Zhao, L.; Shang, W. Damage of full-scale reinforced concrete beams under contact explosion. *Int. J. Impact Eng.* **2022**, *163*, 104180. [[CrossRef](#)]
11. Liu, Y.; Yan, J.; Huang, F. Behavior of reinforced concrete beams and columns subjected to blast loading. *Def. Technol.* **2018**, *14*, 550–559. [[CrossRef](#)]
12. Gao, C.; Kong, X.; Fang, Q. Experimental and numerical investigation on the attenuation of blast waves in concrete induced by cylindrical charge explosion. *Int. J. Impact Eng.* **2023**, *174*, 104491. [[CrossRef](#)]
13. Wei, W.; Rui-chao, L.I.U.; Biao, W.U.; Lin, L.I.; Jia-rong, H.; Xing, W. Damage Criteria of Reinforced Concrete Beams under Blast Loading. *Acta Armamentarii* **2016**, *37*, 1421–1429.
14. Cudzilo, S.; Kohlicek, P.; Trzcinski, V.A.; Zeman, S. Performance of emulsion explosives. *Combust. Explos. Shock Waves* **2002**, *38*, 463–469. [[CrossRef](#)]
15. Simoens, B.; Lefebvre, M.H.; Minami, F. Influence of different parameters on the TNT-equivalent of an explosion. *Cent. Eur. J. Energetic Mater.* **2011**, *8*, 53–67.
16. Locking, P.M. TNT equivalence—Experimental comparison against prediction. In Proceedings of the 27th International symposium on ballistics, Freiburg, Germany, 22–26 April 2013; pp. 22–26.
17. Xie, L.X.; Lu, W.B.; Zhang, Q.B.; Jiang, Q.H.; Chen, M.; Zhao, J. Analysis of damage mechanisms and optimization of cut blasting design under high in-situ stresses. *Tunn. Undergr. Space Technol.* **2017**, *66*, 19–33. [[CrossRef](#)]
18. Wang, H.; Wang, Z.; Wang, J.; Wang, S.; Wang, H.; Yin, Y.; Li, F. Effect of confining pressure on damage accumulation of rock under repeated blast loading. *Int. J. Impact Eng.* **2021**, *156*, 103961. [[CrossRef](#)]
19. Borrvall, T.; Riedel, W. The RHT concrete model in LS-DYNA. In Proceedings of the 8th European LS-DYNA User Conference, Strasbourg, France, 23–24 May 2011; pp. 23–24.
20. Malvar, L.J. Review of static and dynamic properties of steel reinforcing bars. *ACI Mater. J.* **1998**, *95*, 609–616.
21. Cheng, D.-S.; Hung, C.-W.; Pi, S.-J. Numerical Simulation of Near-Field Explosion. *J. Appl. Sci. Eng.* **2013**, *16*, 61–67. [[CrossRef](#)]

Disclaimer/Publisher’s Note: The statements, opinions and data contained in all publications are solely those of the individual author(s) and contributor(s) and not of MDPI and/or the editor(s). MDPI and/or the editor(s) disclaim responsibility for any injury to people or property resulting from any ideas, methods, instructions or products referred to in the content.